Multiparameter Raman Lidar Measurements for the Characterization of a Dry Stratospheric Intrusion Event

PAOLO DI GIROLAMO AND DONATO SUMMA

Dipartimento di Ingegneria e Fisica dell'Ambiente, Università degli Studi della Basilicata, Potenza, Italy

ROSSELLA FERRETTI

Dipartimento di Fisica-CETEMPS, Università degli Studi dell'Aquila, Coppito, L'Aquila, Italy

(Manuscript received 12 November 2008, in final form 7 April 2009)

ABSTRACT

The University of Basilicata Raman lidar system (BASIL) is operational in Potenza, Italy, and it is capable of performing high-resolution and accurate measurements of atmospheric temperature and water vapor based on the application of the rotational and vibrational Raman lidar techniques in the ultraviolet region. BASIL was recently involved in the 2005 International Lindenberg campaign for Assessment of Humidity and Cloud Profiling Systems and Its Impact on High-Resolution Modeling (LAUNCH 2005) experiment held from 12 September to 31 October 2005. A thorough description of the technical characteristics, measurement capabilities, and performances of BASIL is given in this paper. Measurements were continuously run between 1 and 3 October 2005, covering a dry stratospheric intrusion episode associated with a tropopause folding event. The measurements in this paper represent the first simultaneous Raman lidar measurements of atmospheric temperature, water vapor mixing ratio, and thus relative humidity reported for an extensive observation period (32 h).

The use of water vapor to trace intruded stratospheric air allows the clear identification of a dry structure (~1 km thick) originating in the stratosphere and descending in the free troposphere down to ~3 km. A similar feature is present in the temperature field, with lower temperature values detected within the dry-air tongue. Relative humidity measurements reveal values as small as 0.5%–1% within the intruded air. The stratospheric origin of the observed dry layer has been verified by the application of a Lagrangian trajectory model. The subsidence of the intruding heavy dry air may be responsible for the gravity wave activity observed beneath the dry layer.

Lidar measurements have been compared with the output of both the fifth-generation Pennsylvania State University–National Center for Atmospheric Research (PSU–NCAR) Mesoscale Model (MM5) and the European Centre for Medium-Range Weather Forecasts (ECMWF) global model. Comparisons in terms of water vapor reveal the capability of MM5 to reproduce the dynamical structures associated with the stratospheric intrusion episode and to simulate the deep penetration into the troposphere of the dry intruded layer. Moreover, lidar measurements of potential temperature are compared with MM5 output, whereas potential vorticities from both the ECMWF model and MM5 are compared with estimates obtained combining MM5 model vorticity and lidar measurements of potential temperature.

1. Introduction

According to the Brewer–Dobson model (Brewer 1949), circulation in the upper troposphere and stratosphere can be described as an organized upward mass transport from the troposphere to the stratosphere in the tropics followed by a transport to the extratropics in the stratosphere and a downwelling from the stratosphere to the troposphere at middle and high latitudes (Holton et al. 1995). Tropopause folds are the dominant and most efficient mechanism of stratosphere–troposphere exchange (STE) in the middle latitudes. Tropopause folds are events in which the boundary between the stratosphere and the troposphere temporary folds into the troposphere, frequently leading to dynamical instability, enhanced turbulence (Shapiro 1980), and chemical

Corresponding author address: Dr. Paolo Di Girolamo, Viale dell'Ateneo Lucano n. 10, 85100 Potenza, Italy.
E-mail: digirolamo@unibas.it

DOI: 10.1175/2009JTECHA1253.1

mixing between the two layers. Tropopause folds lead to the intrusion into the troposphere of stratospheric air that sinks into the baroclinic zone beneath the upper-tropospheric jet stream. Folds usually take place on the western flank of cut-off low systems. Clean, dry stratospheric air, rich in ozone and potential vorticity (PV), is transported downward to tropospheric levels. Stratospheric air intruding into the troposphere forms filamentary features in ozone (Reid and Vaughan 1991; Galani et al. 2003), water vapor (Appenzeller and Davies 1992), and temperature profiles. These filaments can subside deep into the troposphere (Stohl and Trickl 1999), triggering severe weather events (Massacand et al. 2001) and high wind speeds at the surface (Goering et al. 2001). Finally, these features are destroyed by turbulence (Shapiro 1980), which can be generated by convection, breaking gravity waves, and wind shear. The lifetime of the filaments is also influenced by radiation (Forster and Wirth 2000) and molecular diffusion, which ultimately determine the time scales of dry stratospheric air mixing with surrounding tropospheric air (Shapiro 1980).

Raman lidars with water vapor and temperature measurement capabilities are very suitable tools to resolve the spatial and temporal scales of these atmospheric features and to provide information about their evolution. The use of these systems allows us to accurately trace stratospheric air intruding into the troposphere. In this study, we illustrate and discuss the measurements carried out by a rotational–vibrational Raman lidar system to characterize a stratospheric air intrusion event on its way down to the lower troposphere. Water vapor lidar measurements during stratospheric intrusions and tropopause fold events have been reported by Hoinka et al. (2003), D'Aulerio et al. (2004), Flentje et al. (2005), and Di Girolamo et al. (2008). However, the present paper represents, to our knowledge, the first reported measurements of these phenomena based on the application of a lidar system with both water vapor and temperature measurement capabilities. Simultaneous atmospheric temperature and water vapor mixing ratio measurements, and consequently relative humidity, are reported and discussed for an extensive observation period (32 h) covering nighttime, daytime, and the transitions between the two.

In this paper, the rotational and the vibrational Raman lidar techniques are applied for the first time together in a UV lidar system, making this a completely eye-safe system. Previous papers reporting simultaneous lidar measurements of both rotational and vibrational Raman scattering performed by a single lidar system or by collocated lidar systems were based on measurements in the visible (532 nm; see, e.g., Mattis et al. 2002). It is noteworthy that the UV region is safer than the visible region in terms of hazard for eye injury, with a threshold for the thermal retinal damage that is 3–4 orders of magnitude lower. Specifically, the maximum allowed exposition of the human eye to 1–100-ns laser pulses is 31–100 J m^{-2} in the spectral region of 315–400 nm, whereas it is only 5 mJ m^{-2} in the 400–700-nm region (IEC 2001). UV laser beams used in most lidar applications, as in the present system, result to be eye safe within a few hundred meters of the laser source.

Although stratosphere–troposphere exchange processes associated with midlatitude tropopause folding episodes have been widely studied over the last four decades using both observations and numerical models (e.g., review in Stohl et al. 2003), a limited number of papers focuses on the study of the evolution of deep intrusion events based on both measurements and modeling (e.g., Cristofanelli et al. 2003; Roelofs et al. 2003; Zanis et al. 2003; Flentje et al. 2005). In this paper, lidar measurements are compared in terms of water vapor mixing ratio with simulations from the fifth-generation Pennsylvania State University–National Center for Atmospheric Research (PCU–NCAR) Mesoscale Model (MM5) and the European Centre for Medium-Range Weather Forecasts (ECMWF) global model and in terms of potential temperature with MM5. Additionally, potential vorticity computations from both ECMWF and MM5 are compared with estimates obtained combining MM5 model vorticity and the lidar measurements of potential temperature.

The paper is organized as follows: In section 2, we briefly describe the Raman lidar system setup and the methods of analysis and calibration of lidar data. In section 3, a brief description of the mesoscale model is provided, and the meteorological situation is described in section 4. Results are outlined and discussed in section 5 and summarized in section 6.

2. BASIL

Lidar measurements presented in this paper were performed in Potenza, Italy (40°38′45″N, 15°48′32″E, 730 m above mean sea level), by the University of Basilicata Lidar system (BASIL) from the Department of Environmental Engineering and Physics (DIFA). The major feature of BASIL is represented by its capability to perform high-resolution and accurate measurements of atmospheric temperature, in both daytime and nighttime, based on the application of the rotational Raman lidar technique in the UV (Behrendt and Reichardt 2000; Di Girolamo et al. 2004; Behrendt 2005; Di Girolamo et al. 2006). Besides temperature, BASIL is capable to provide measurements of particle backscatter at 355 and 532 nm, particle extinction at 355 nm, particle

TABLE 1. Interference filter specifications.

Selected signal	Center wavelength (nm)	Bandwidth, FWHM (nm)	Blocking at 355 nm
Rayleigh–Mie at 355 nm	354.7	1.0	—
Rayleigh–Mie at 532 nm	532	1.0	10^{-6}
N_2 Raman	386.7	1.0	10^{-10}
H_2O Raman	407.5	0.25	10^{-12}
Lo*J* rotational Raman	354.3	1.0	10^{-8}
Hi*J* rotational Raman	352.9	0.2	10^{-8}

depolarization at 355 nm, and water vapor mixing ratio (Whiteman 2003a,b) in both daytime and nighttime. Relative humidity measurements are obtained from the simultaneous measurements of water vapor and temperature. This wide set of measured parameters makes this system particularly suited for the study of meteorological processes and the characterization of aerosol and cloud microphysical properties.

The experimental setup of BASIL was described in few previous papers (Maestri et al. 2009, submitted to *Atmos. Res.*; Griaznov et al. 2007; Fiorucci et al. 2008). However, more detailed descriptions of the system design, methods of data analysis, procedures for calibration, and characteristics of the lidar system uncertainty in terms of both random and systematic errors are provided here.

BASIL makes use of a neodymium-doped yttrium aluminium garnet (Nd:YAG) laser source equipped with second and third harmonic generation crystals and capable of emitting pulses at 355 and 532 nm, with single pulse energies of 250 and 300 mJ, respectively; a pulse repetition rate of 20 Hz; and a pulse duration of 5–6 ns. The beam divergence is 0.5 mrad [full width at half maximum (FWHM)] and the beam diameter is 8 mm. Laser beams at 355 and 532 nm are simultaneously transmitted in the atmosphere along the zenith. To meet eye-safety requirements, only a small fraction of the 532-nm laser energy (5 mJ) is transmitted into the atmosphere, whereas the remainder is sent into an optical dump. Considering 5 mJ m^{-2} as the maximum allowed exposition of the human eye to 5–6-ns laser pulses at 532 nm (IEC 2001), eye-safety conditions are reached at 2250 m. On the contrary, the laser beam at 355 nm is transmitted unattenuated. In fact, considering a maximum allowed exposition of 50 J m^{-2} to 5–6 ns laser pulses at 355 nm, eye-safety conditions are reached within 160 m of the laser source.

The receiver is built around a telescope in Newtonian configuration (40-cm diameter primary mirror). Collected radiation is split into eight portions by means of dichroic or partially reflecting mirrors; specifically, two portions are fed into the detection channels used for temperature measurements; two other portions are sent to the water vapor and nitrogen Raman channels; another two portions are fed into the 355- and 532-nm elastic channels; and a fraction of the signal entering the 355-nm channel is split into two additional portions to allow the detection of the parallel and cross-polarized elastic signals used for the determination of particle depolarization. Signal selection is performed by means of narrowband interference filters, whose specifications are reported in Table 1. Signal detection is accomplished by means of photomultipliers located in cascade with each interference filter, whereas detected signals are sampled by means of photon-counting units. The vertical and temporal resolutions of the rough data are 30 m and 1 min, respectively. A block diagram of the system is provided in Fig. 1.

The photon-counting electronics used in BASIL for signal detection has a maximum measurable count rate of 350 MHz, which corresponds to a minimum pulse-pair resolution time of 2.9 ns. For count rates higher than 10 MHz, a count-saturation correction scheme has to be applied to correct for the nonlinear response of these devices. Assuming the counting system to be nonparalyzable, the following correction algorithm is used:

$$N_{\text{real}} = \frac{N_{\text{obs}}}{1 - \tau N_{\text{obs}}}, \tag{1}$$

where N_{obs} is the observed count rate; N_{real} is the actual count rate; and τ is the value of the resolving time, also called counting system dead time. This correction scheme is usually applied to N_2 Raman signals and rotational Raman signals up to an altitude of ~4 km. In the determination of counting system resolving time, contributions from different components of the receiving system must be considered, with photomultipliers usually playing an important role. The considered photomultipliers have a very short rise of 0.7 ns for an overall pulse width not exceeding 2 ns (FWHM), which characterizes them as high-speed response photomultipliers. This value is less than the nominal resolving time of the counting system (2.9 ns). The resolving time of each photomultiplier/discriminator/counting unit was determined empirically based on the procedure originally proposed by Donovan et al. (1993), as modified by

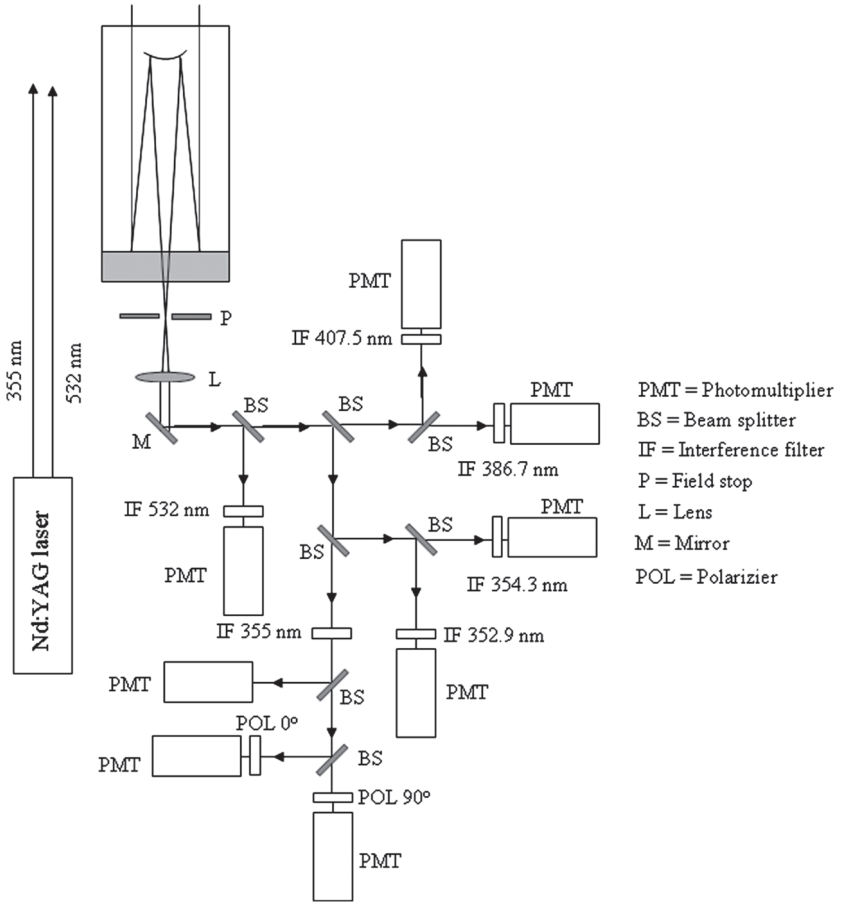

FIG. 1. Block diagram of BASIL experimental setup.

Whiteman et al. (1992) and Whiteman (2003a). For this purpose, we considered two sets of atmospheric signals: full-strength signals and signals acquired with 20% neutral density filters in front of the detector. An assumption was made that the same atmospheric and instrumental conditions were present during the measurement of both signals. The nonparalyzable correction algorithm in expression (1) was applied to both the full- and reduced-strength signals, considering different values of the resolving time. We tested values of τ in the range of 2.0–3.0 ns, with steps of 0.2 ns. The ratio of the count-corrected reduced-strength signals to the count-corrected full-strength signals was then computed for the different values of τ. For each photomultiplier, the resolving time value that yields curves that are most nearly constant with altitude was the chosen value for final correction. Determined values are found to be in the range of 2.8–3.0 ns.

The correction algorithm in expression (1) is applicable when the true count rate is not exceeding τ^{-1} (Mielke 2005). The maximum observed count rate that was experienced during the present measurements was ~130 MHz, whereas typical values during measurements were much smaller (50 MHz). Considering a resolving time τ of 2.9 ns, the maximum correction factor is 1.61 and the maximum true count rate is 210 MHz, whereas the typical correction factor and typical true count rate are 1.17 and 58 MHz, respectively. Maximum and typical true count rates are well below the value of τ^{-1} (350 MHz) indicated by Mielke. An error of ± 0.1 ns in the estimate of τ may lead to a systematic error in water vapor mixing ratio measurements of 3% and 0.7% at maximum and typical count rate levels, respectively. However, it is to be noticed that the correction algorithm in expression (1) is applied before the calibration procedure (illustrated later); thus, potential systematic errors in the application of the correction algorithm are removed in the calibration procedure and residual errors associated with the application of the count-saturation correction scheme are finally included inside the calibration error (3%–5%).

Temperature measurements are performed by BASIL through the application of the rotational Raman lidar technique in the UV (Di Girolamo et al. 2004), which is based on the detection of pure rotational Raman

scattering from oxygen and nitrogen molecules in the proximity of the laser wavelength ($\lambda_{loJ} = 354.3$ nm and $\lambda_{hiJ} = 352.9$ nm). Atmospheric temperature can be obtained from the power ratio of high-to-low quantum number rotational Raman signals $R(T)$ through the application of the analytical expression

$$R(T) = \frac{P_{hiJ}(z[T])}{P_{loJ}(z[T])} \cong \exp\left(\frac{\alpha}{T} + \beta\right), \quad (2)$$

where $P_{loJ}(z)$ and $P_{hiJ}(z)$ are the background-subtracted low (lo$J$) and high (hi$J$) quantum number rotational Raman signal intensities, respectively, from the scattering volume at altitude z in the anti-Stokes branch.

The calibration function $\exp(\alpha/T + \beta)$ in Eq. (2), exactly valid for two individual lines, is in good approximation also valid for BASIL, where rotational Raman signals includes several lines. The calibration constants α and β in Eq. (2) can be determined through the comparison of lidar data with simultaneous and collocated measurements (e.g., radiosonde data). In the case of BASIL, radiosondes (Vaisala RS92) released from the nearby Italian National Research Council (CNR) Institute of Methodologies for Environmental Analysis (IMAA) ground station (8.2 km away; west–southwest direction) were considered and the comparison was carried out for an extended measurement sample in the altitude region up to 5–10 km above mean sea level (in what follows, when not specified, altitudes are intended above mean sea level).

The Raman lidar technique for the determination of the water vapor mixing ratio profile has been extensively discussed in literature (for a review, see Whiteman 2003a,b). The water vapor mixing ratio $x_{H_2O}(z)$ can be obtained from the power ratio of water vapor to molecular nitrogen vibrational Raman signals through the application of the analytical expression

$$x_{H_2O}(z) = k\frac{P_{H_2O}(z)}{P_{N_2}(z)}\Delta T_{\lambda_{H_2O},\lambda_{N_2}}, \quad (3)$$

where $P_{H_2O}(z)$ and $P_{N_2}(z)$ are the background-subtracted water vapor and molecular nitrogen Raman signal intensities, respectively; k is the lidar system calibration coefficient; and $\Delta T_{\lambda_{H_2O},\lambda_{N_2}}$ is the differential transmission term, which accounts for the different atmospheric transmission at the two Raman wavelengths $\lambda_{H_2O} = 407.5$ nm and $\lambda_{N_2} = 386.7$ nm. Here, $\Delta T_{\lambda_{H_2O},\lambda_{N_2}}$ is primarily caused by Rayleigh scattering and can easily be determined based on the use of radiosonde or standard-atmospheric profiles of number density. For the present measurements, we considered collocated radiosonde launches and number density profiles at the times and altitudes of the lidar data were obtained from linear interpolation of the radiosonde data (more details on this interpolation procedure are illustrated in section 5, when discussing Fig. 11). An additional component of $\Delta T_{\lambda_{H_2O},\lambda_{N_2}}$ is associated with wavelength dependence of particle extinction, which is usually very small (1%–2%); for the present measurements, this component was determined from simultaneous and collocated lidar measurements of particle extinction at 355 nm based on the procedure proposed by Whiteman (2003b). The error affecting the estimate of $\Delta T_{\lambda_{H_2O},\lambda_{N_2}}$ is found to not exceed 1%.

The use of narrowband interference filters for the selection of the H_2O and N_2 Raman signals requires a proper accounting for the temperature dependence of H_2O and N_2 Raman scattering. For the filter configuration of BASIL (filter widths $\Delta\lambda_{H_2O} = 0.25$ nm and $\Delta\lambda_{N_2} = 1.0$ nm FWHM), the magnitude of this effect varies from 0% to 2.5% in the temperature range observed between the surface and 10 km (Whiteman 2003a). To remove this systematic effect, a height-dependent correction term was applied to the data (Whiteman 2003a). This correction term was determined from simultaneous temperature lidar measurements (Whiteman 2003a; Whiteman et al. 2006), assuming the interference filters to have a Gaussian shape (the filter specs in terms of center wavelength and width are included in Table 1) and considering the Raman spectroscopic information reported in Avila et al. (1999). The residual error after correction is expected to not exceed 0.5%.

The calibration coefficient k, for BASIL, was determined by comparing water vapor mixing ratio data from lidar and radiosondes for an extended measurement sample in the altitude region of 3–7 km. For this purpose, the radiosondes released from the nearby IMAA ground station were considered again. The selection of the altitude region of 3–7 km comes from the necessity to exclude boundary layer data from the comparison because, in the boundary layer, the effects of water vapor heterogeneity may be large for the two sites, which are 8.2 km apart.

Relative humidity over water RH(z) is defined as

$$\mathrm{RH}(z) = \frac{e(z)}{e_{S_{H_2O}}(z)}, \quad (4)$$

where $e(z)$ is the vertical profile of the water vapor partial pressure and $e_{S_{H_2O}}(z)$ is the vertical profile of the saturation pressure over water. The water vapor partial pressure $e(z)$ is related to the water vapor mixing ratio $x_{H_2O}(z)$ through the expression (Mattis et al. 2002)

$$e(z) = \frac{x_{H_2O}(z)p(z)}{\varepsilon + x_{H_2O}(z)}, \quad (5)$$

where $\varepsilon = 0.622$ and $p(z)$ is the atmospheric pressure. Based on recommendations from World Meteorological Organization (WMO 2000, appendix A), $e_{S_{H_2O}}(z)$ can be expressed as

$$e_{S_{H_2O}}(z) = 10^{\{a[1-273.16/T(z)]+b\mathrm{Log}[T(z)/273.16]+c[1-10^{d(T(z)/273.16-1)}]+e[10^{f(1-273.16/T(z))}-1]+g\}}, \quad (6)$$

where $a = 10.79574$, $b = -5.02800$, $c = 1.50475 \times 10^{-4}$, $d = -8.2969$, $e = 0.42873 \times 10^{-3}$, $f = -4.769955$, and $g = 0.78614$.

The value of $e_{S_{H_2O}}(z)$ depends solely on atmospheric temperature $T(z)$, which is measured by BASIL, whereas $e(z)$ can be obtained from $x_{H_2O}(z)$, again measured by BASIL, and $p(z)$ can be obtained from radiosonde data or from surface pressure measurements hydrostatically scaled to the lidar altitude levels z. In the present work, we considered pressure information from radiosondes; pressure profiles at the times and altitudes of the lidar data were obtained from linear interpolation of the radiosonde data (more details on this interpolation procedure are illustrated in section 5, when discussing Fig. 11).

The use of a very compact optical design reduces significantly the differences between the overlap functions of the H_2O and N_2 Raman signals used to estimate the water vapor mixing ratio. Nevertheless, small differences between the two overlap functions in the lower 1500 m may be quantified through the application of the so-called N_2 calibration procedure (Whiteman et al. 1992), which consists of the use of an N_2 Raman filter in both the H_2O and N_2 channels. In the application of this procedure, if dichoric mirrors are used for the partitioning of the signals, then these have to be removed to eliminate potential polarization effects and they must be substituted by partially reflecting mirrors, which have transmission efficiencies that are wavelength and polarization independent. In the present system, the beam splitter used to separate the H_2O and N_2 Raman signals is characterized by a high reflectivity (~90%), which guarantees that most of the H_2O Raman signal is deflected into the H_2O Raman channel, and a low transmission (~10%), which allows to feed a limited portion of the N_2 Raman signal—which is too strong and needs to be attenuated in any case—into the N_2 Raman channel. This calibration procedure is applied at the beginning and end of each measurement session of BASIL. In case of high water vapor horizontal homogeneity, an alternative estimate of the overlap function ratio is obtained from the comparison of lidar with simultaneous and collocated radiosonde measurements. Estimates of the overlap function from these two calibration procedures have been compared and deviations from the two estimates were found to not exceed 2%.

Similar calibration procedures are applied to quantify possible differences in the overlap functions of the rotational Raman signals used to estimate atmospheric temperature. A first procedure consists in inverting the two rotational Raman filters and comparing the retrieved temperature profiles before and after the inversion of the filters. This calibration procedure, as the analogous used for the water vapor channels, is applied at the beginning and end of each measurement session. Again, in case of high horizontal homogeneity, an alternative estimate of the overlap function ratio is obtained from the comparison of lidar with simultaneous and collocated radiosonde measurements.

Lidars provide profiles of the atmospheric parameters with accurate information of the statistical measurement uncertainty. Statistical uncertainty is estimated through the application of Poisson statistics, which is well suited in cases of data acquired in photon-counting mode, as in the case of BASIL.

The statistical error affecting temperature measurements can be determined through the following analytical expression (Behrendt and Reichardt 2000; Di Girolamo et al. 2004):

$$\Delta T(z) = \frac{\partial T(z)}{\partial R} R(z) \sqrt{\frac{P_{\mathrm{lo}J}(z) + \mathrm{bk}_{\mathrm{lo}J}}{P^2_{\mathrm{lo}J}(z)} + \frac{P_{\mathrm{hi}J}(z) + \mathrm{bk}_{\mathrm{hi}J}}{P^2_{\mathrm{hi}J}(z)}}, \quad (7)$$

where the terms $\mathrm{bk}_{\mathrm{lo}J}$ and $\mathrm{bk}_{\mathrm{hi}J}$ represent the sky background signals collected in the low- and high-J channels, respectively. This expression assumes detector noise to be negligible. A similar expression applies for the percent statistical error affecting the water vapor mixing ratio measurements (Whiteman 2003b):

$$\frac{\Delta x_{H_2O}(z)}{x_{H_2O}(z)} = 100 \times \sqrt{\frac{P_{H_2O}(z) + \mathrm{bk}_{H_2O}}{P^2_{H_2O}(z)} + \frac{P_{N_2}(z) + \mathrm{bk}_{N_2}}{P^2_{N_2}(z)}}, \quad (8)$$

where the terms bk_{H_2O} and bk_{N_2} represent the sky background signals collected in the water vapor an molecular nitrogen channels. The random error affecting relative

humidity measurements can then be determined from the random uncertainty affecting temperature and water vapor mixing ratio measurements through the expression (Mattis et al. 2002)

$$\Delta \mathrm{RH}(z) = \sqrt{\left(\frac{\partial \mathrm{RH}}{\partial e}\frac{\partial e}{\partial x_{\mathrm{H_2O}}}\right)^2 \Delta x^2_{\mathrm{H_2O}}(z) + \left(\frac{\partial \mathrm{RH}}{\partial e_s}\frac{\partial e_s}{\partial T}\right)^2 \Delta T^2(z)}. \quad (9)$$

This expression neglects the error contribution associated with pressure uncertainties, which is much smaller than the other terms.

Statistical errors for temperature, water vapor mixing ratio, and relative humidity measurements are represented in Figs. 2a–c, respectively. Nighttime and daytime performances are determined for the dataset under consideration. Specifically, nighttime performances were determined at 0000 UTC 2 October 2005, whereas daytime performances were determined at 0700 UTC 2 October 2005. Vertical and temporal resolutions can be traded-off to improve measurement precision, with random error in Eqs. (7)–(9) being inversely proportional to the square root of both the vertical and temporal resolutions. Precision estimates in Figs. 2a–c are based on vertical and temporal resolutions of 300 m and 10 min, respectively.

For nighttime operation, the statistical uncertainty affecting temperature measurements $\Delta T(z)$ is between 0.2 and 1 K up to 7.5 km and is less than 1.5 K up to 9 km. For daytime operation, $\Delta T(z)$ is less than 1 K up to 5.5 km and less than 5 K up to 8 km, with a maximum precision of 0.2 K at 1.6–2.0 km. At nighttime, the percent random error affecting water vapor mixing ratio measurements, $\Delta x_{\mathrm{H_2O}}(z)/x_{\mathrm{H_2O}}(z)$, is less than 1% up to 3 km and less than 10% up to 9 km. For daytime operation, $\Delta x_{\mathrm{H_2O}}(z)/x_{\mathrm{H_2O}}(z)$ is less than 20% up to 5.5 km (with the only exception of the data points within the dry layer, where values reach up to ~50%) and less than 100% up to 8.5 km. The random error for relative humidity measurements, $\Delta \mathrm{RH}(z)$, at night, is less than 3% up to 6.7 km and less than 5% up to 9 km, with $\Delta \mathrm{RH}(z) < 1\%$ between 1.8 and 5 km and with values not exceeding 0.5% in the dry layer. For daytime operation, $\Delta \mathrm{RH}(z)$ is less than 3% up to 4 km and less than 10% up to 5.5 km, with values not exceeding 0.5% in the dry layer. Finally (not shown), random error affecting night time particle backscatter measurements at 355 nm is ~5% up to 2 km and less than 20% up 10 km, whereas for daytime measurements it is <10% up to 2 km and less than 30% up 10 km; random error affecting nighttime particle extinction measurements is 5% up to 2 km and less than 20% up 10 km, whereas for daytime measurements it is <10% up to 2 km and less than 50% up 10 km.

Besides random errors, which limit measurement precision, several sources of systematic error have to be considered to assess measurement accuracy. In temperature measurements, laser frequency fluctuations resulting from thermal drifts inside the laser cavity (~0.1 $\mathrm{cm^{-1}\ K^{-1}}$) can lead to a systematic bias not exceeding 0.1 K (Di Girolamo et al. 2004), whereas filter position drifts associated with thermal drifts are also <0.1 K for filters contained in a thermally controlled environment (Di Girolamo et al. 2006). A bias of ~0.2 K is associated with the uncertainty in the estimate of the calibration coefficients [radiosonde biases, different air masses being sensed by the radiosonde and the lidar, and the assumption of the calibration function in Eq. (2) to be valid for large portions of the rotational Raman spectrum]; this uncertainty includes the residual error associated with the application of the count-saturation correction scheme already discussed. An additional bias source may be associated with slight receiver misalignments leading to different overlap functions in the two RR channels [as mentioned earlier, this may lead to an additional uncertainty of 1%–2% in the overlap region (i.e., in the lowermost 1.5 km), which translates into a temperature bias of <2 K].

In water vapor mixing ratio measurements, a systematic error is associated with the estimate of the calibration coefficient (3%–5%), again including the residual error associated with the application of the count-saturation correction scheme already discussed. An additional bias (<0.5%) is associated with the use of narrowband filters (see earlier discussion). The systematic errors associated with the determination of the differential transmission term $\Delta T_{\lambda_{\mathrm{H_2O}}}$ is less than 1%, whereas the residual bias after correcting for differences in the overlap functions of the H_2O and N_2 Raman signals (important only in the lowermost 1.5 km) is less than 2%.

3. Mesoscale modeling

MM5, version 3 (Grell et al. 1994; Dudhia 1993) was operationally running over Italy at Centro di Eccellenza Tecniche di Telerilevamento e Modellistica Numerica per la Previsione di Eventi Meteo Severi (CETEMPS)–University of Aquila during the 2005 International

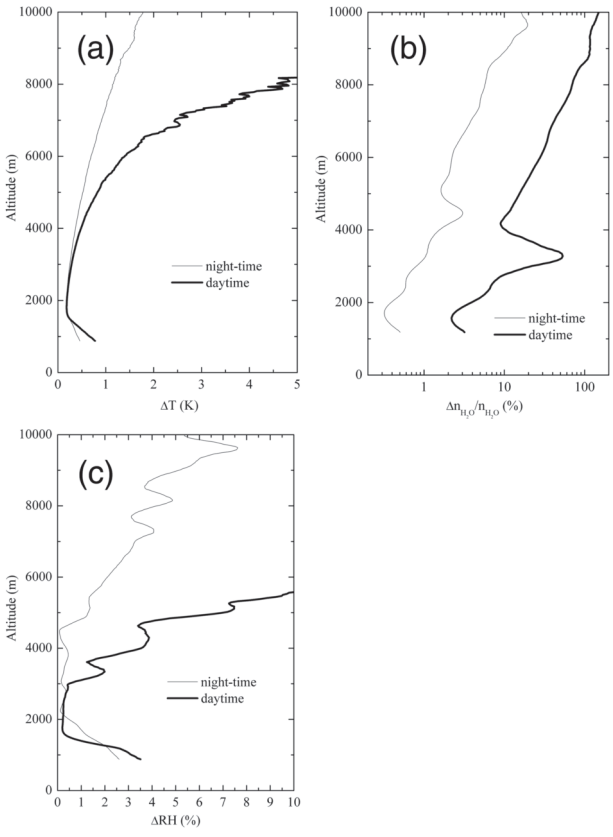

FIG. 2. (a) Random error affecting temperature, (b) water vapor mixing ratio, and (c) relative humidity measurements by BASIL for nighttime (0000 UTC 2 Oct 2005) and daytime operation (0700 UTC 2 Oct 2005). Precision estimates are based on vertical and temporal resolutions of 300 m and 10 min, respectively.

Lindenberg campaign for Assessment of Humidity and Cloud Profiling Systems and Its Impact on High-Resolution Modeling (LAUNCH 2005). MM5 is a limited-area, nonhydrostatic, terrain-following sigma-coordinate model designed to simulate or predict mesoscale and regional-scale atmospheric circulation. The configuration used for this study, based on CETEMPS group knowledge, is as follows (Paolucci et al. 1999): 3 two-way nested domains (grid size is 27 km for the mother domain D1, whereas it is 9 and 3 km for the nested domains D2 and D3, respectively) with high resolution over southern central Italy (Fig. 3) and 29 vertical sigma levels from the surface to 100 hPa. The Medium-Range Forecast parameterization for the PBL (Troen and Marht 1986) is used together with convective parameterization (Kain and Fritsch 1993; Ferretti et al. 2000) on domains D1 and D2. The Reisner1 (Reisner et al. 1998; Serafin and Ferretti 2007) mixed-phase scheme is used as a resolvable-scale microphysics scheme. Radiative parameterization accounts for longwave and shortwave interactions with explicit cloud and clear air, yielding atmospheric temperature tendencies and surface radiation fluxes. As noted in the results section, a higher-resolution simulation is also performed to better highlight the wave structure over BASIL. For this specific simulation, the domain configuration is modified with the addition of a higher-resolution domain (grid size = 1 km) centered over Potenza.

The ECMWF analyses are used for the initial and boundary conditions; the model simulation considered in this study starts at 1800 UTC 1 October and lasts for 48 and 33 h for the 3- and 1-km-resolution runs, respectively. The MM5 meteorological fields are compared with lidar measurements, and the results are discussed in the following sections. Model simulations are performed without assimilating lidar measurements, because they are used only for comparison. Moreover, the assessment of the impact of the assimilation of lidar data on model output (Wulfmeyer et al. 2006; Grzeschik et al. 2008) is out of the goals of this work and will be the objective of a forthcoming paper based on the use of data from multiple lidar stations.

4. Meteorological situation

Besides the MM5 model domains, Fig. 3 also shows the Spinning Enhanced Visible and Infrared Imager (SEVIRI) channel 5 image for 1800 UTC 1 October 2005, which reveals the cold dry air entering central Italy from the east and then moving southeastward (dark tongue in the figure). SEVIRI channel 5 covers the spectral range 5.35–7.15 μm, which includes a major absorption band for water vapor, and it is primarily used to monitor water vapor in the upper troposphere, with a weighting function peaking at ~350 hPa (i.e., ~8 km). The cold air intrusion is associated with intense cyclogenesis over the Tyrrhenian Sea, producing a cut-off low over western Greece. At the same time, heavy precipitations took place in northern Italy, whereas precipitations reached the observation area later on 3 October 2005.

The low-level cyclogenesis and the upper-level cut-off low are clearly shown by the ECMWF analysis of the 500-hPa geopotential height (Fig. 3, red contour lines) and the 850-hPa wind field (Fig. 3, black arrows) at 1800 UTC 1 October 2005. Note that ECMWF relative humidity analysis at 850 hPa (not shown) correctly reproduces the dry-air tongue, but also misplaces it. In fact, the dry-air tongue appears displaced westward (~200 km) with respect to satellite data, as well as with respect to the lidar data illustrated in the next section.

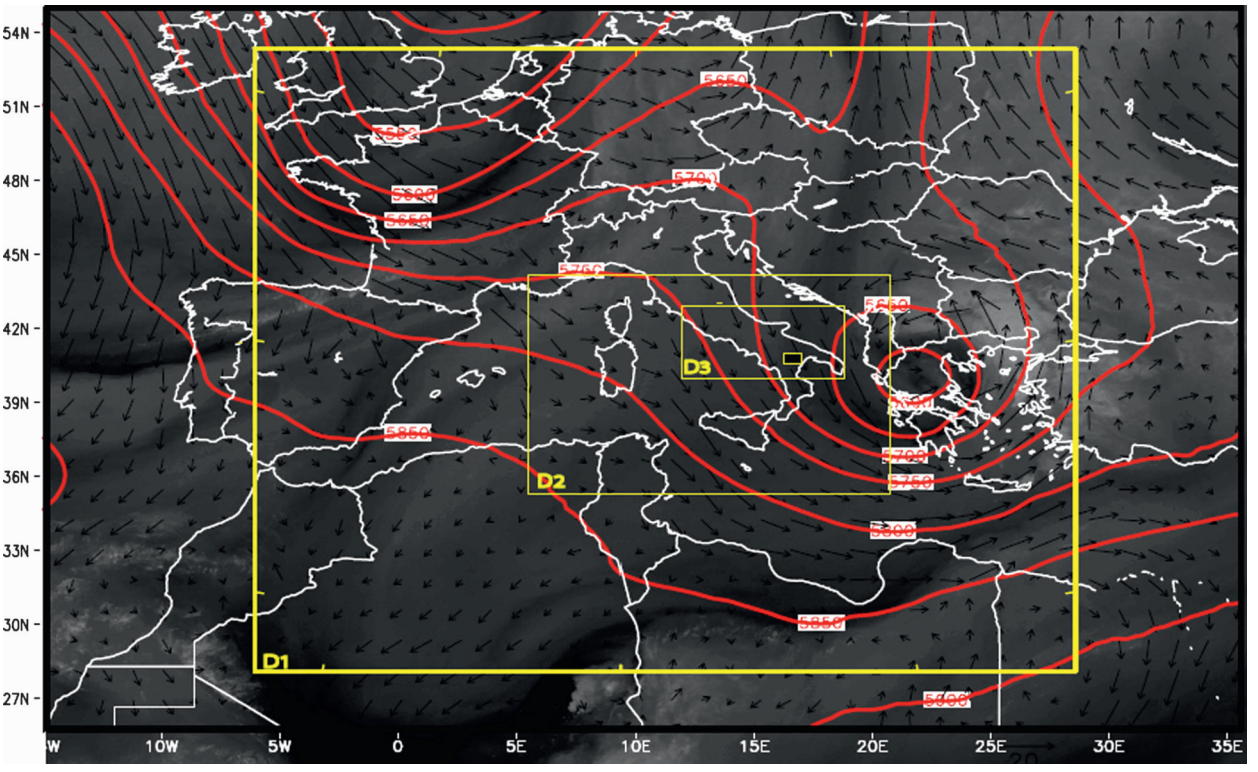

FIG. 3. ECMWF analysis of geopotential height at 500 hPa (red contour lines) and wind field at 850 hPa (black arrows) for 1800 UTC 1 Oct 2005. SEVIRI satellite image (channel 5) for 1800 UTC 1 Oct 2005 is represented as background. MM5 model domains are also illustrated in yellow: D1, with a resolution of 27 km; D2, with a resolution of 9 km; and the innermost D3, with a resolution of 3 km. The lidar location is indicated by the small yellow square.

5. Results

a. *Lidar observations of the intruded stratospheric air and the underlying wave activity*

The measurements illustrated in this paper were performed in the framework of LAUNCH 2005, which was held in the period 12 September–31 October 2005. During this period, BASIL collected ~250 h of measurements distributed over 13 intensive observation periods (IOPs) and 25 days. The main goal of LAUNCH 2005 was the assessment of the impact of variational data assimilation into an operational high-resolution weather forecasting model from a network of ground-based water vapor lidars in comparison to microwave profilers.

Figure 4 illustrates the time evolution of the water vapor mixing ratio over a period of ~32 h from 1805 UTC 1 October to 0215 UTC 3 October 2005. Measurements were stopped shortly afterward because of the onset of thick clouds and precipitation. The figure covers both night-to-day and day-to-night transitions, with the daytime portion clearly distinguishable at the center of the measurement record with noisy data above ~4 km (black regions represent unrealistic values). Figure 4 is plotted as a succession of 10-min-averaged consecutive profiles. To reduce signal statistical fluctuations, vertical smoothing is applied to the data to achieve an overall vertical resolution of 75 m up to 5 km and of 150 m above 5 km. Random error in the nighttime portion is less than 2% up to 3 km and less than 15% up to 9 km, whereas random error in the daytime portion is less than 40% up to 6 km and less than 100% up to 7.5 km.

Two distinct dry laminae are observed between 1805 UTC 1 October and ~0630 UTC 2 October 2005: an upper lamina with a vertical extent of 1–1.5 km showing a descending trend from an initial altitude of 6–7 km down to ~3 km and a lower lamina with an almost-stable altitude of 2–2.5 km and a vertical extent of 0.5–1 km. The upper lamina is found to descend with an apparent fall speed of 220–250 m h^{-1}, and it is identified to be associated with the intrusion of dry stratospheric air, as confirmed by the back-trajectory analysis discussed later in this section (illustrated in Fig. 13). The two laminae appear to merge into a single lamina after 0630 UTC and vanish around 1430 UTC 2 October 2005, possibly destroyed by turbulence generated by convection and breaking gravity waves. Note that the lidar system detects the dry-air tongue as it moves over the system, and

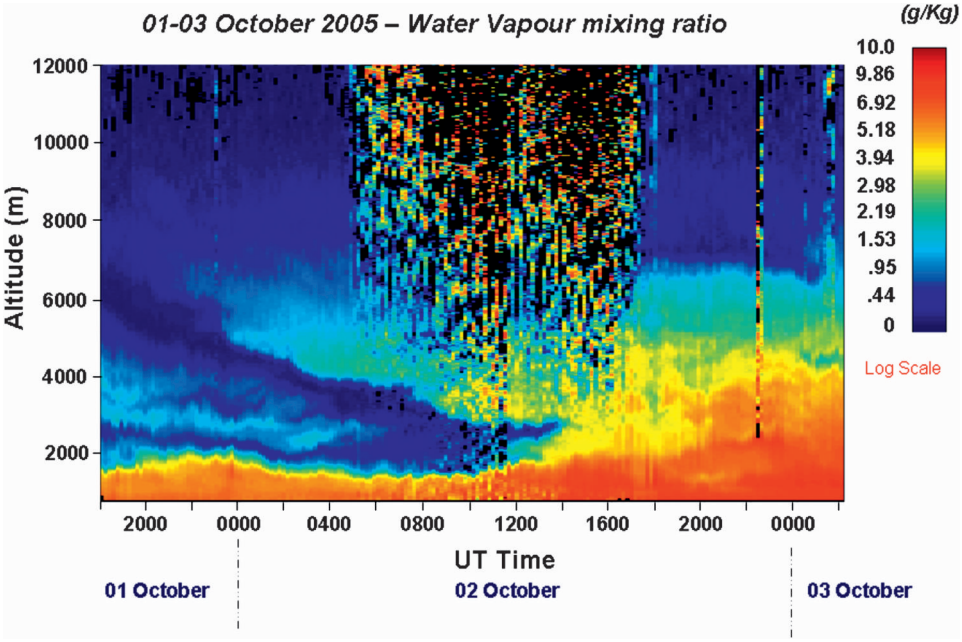

FIG. 4. Time evolution of BASIL water vapor mixing ratio from 1805 UTC 1 Oct to 0215 UTC 3 Oct 2005.

the SEVIRI image at 1500 UTC 2 October (not shown here) indicates that this tongue is still present east of Potenza after it has passed the lidar site. Lidar data are in phase matching with satellite data; in fact, the dry-air tongue is clearly visible in Fig. 3 at the same time (1800 UTC) of the lidar measurements, when the elevated dry layer was first detected at an altitude of 6–7 km. Figure 4 shows large humidity gradients near the intrusion, with very dry air within the intrusion ($q = 0.05$ g kg^{-1}; i.e., 80 ppmv) and very moist air above 3 km before the arrival of the intrusion (q in excess of 2 g kg^{-1}; i.e., 3200 ppmv). Values of q found within the intrusion are consistent with air masses originating in the lowermost stratosphere and progressively mixing while penetrating down through the troposphere (see discussion in section 5b concerning the progressive dilution of the dry intruded stratospheric air based on back-trajectory analysis). Increased values above 3 km before the arrival of the intrusion are consistent with deep convection, which rapidly transports moist air from the PBL into the upper troposphere.

A portion of Fig. 4 that specifically focuses on the nighttime portion of the dry intrusion event is depicted in Fig. 5. This extends for a period of ~14.5 h from 1805 UTC 1 October to 0825 UTC 2 October 2005. Data in this figure are characterized by higher vertical and temporal resolutions (60 m and 1 min, respectively), which allow us to highlight the fine structures of the water vapor field. As a drawback, the selection of higher vertical and temporal resolutions than the ones used in Fig. 4 leads to higher noise levels in the upper troposphere. Figure 5 also illustrates the MM5 model simulation of potential vorticity (black contour lines), vertical wind velocity w (white arrows) and equivalent potential temperature θ_e (gray and black contour lines), and ECMWF model simulation of the tropopause height (yellow line corresponding to 2×10^{-6} m^2 s^{-1} K kg^{-1} surface). The tropopause height is found to decrease during the measurement period, as a result of the folding process. Results reveal that the dry-air intrusion observed in the lidar data is in very good correlation with the MM5 potential vorticity isoline of 1×10^{-6} m^2 s^{-1} K kg^{-1}, with MM5 properly reproducing the dynamical structures associated with the stratospheric intrusion episode.

Lidar data in Fig. 5 also reveal the presence of waves in the low troposphere, which may have been triggered by the subsiding heavy dry air intruded from the stratosphere. Gravity waves can be generated by geostrophic adjustment in the vicinity of a tropopause fold (Zhang et al. 2001; Bertin et al 2001; Koch and Lu 2006). Observed waves may also be generated by flow over mountain ridges (Neiman et al. 2001), as Potenza is surrounded by several low-elevation mountains and orographically induced waves are often observed. The propagation of gravity waves is clearly highlighted by the wavy structure of the humidity filaments observed between 1.5 and 6 km from the beginning of the measurement period to approximately 0000 UTC 2 October 2005.

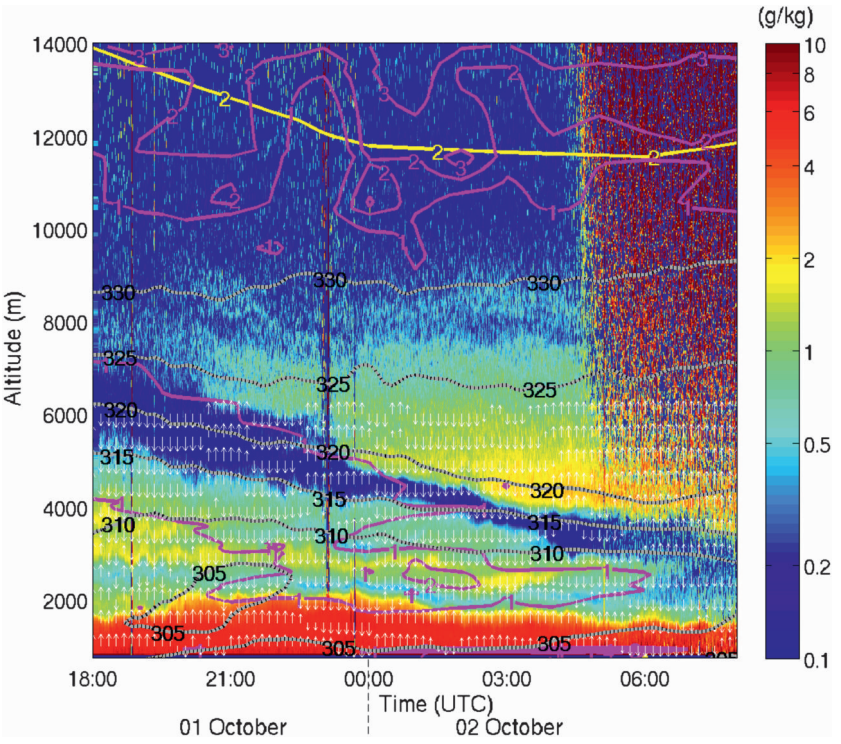

FIG. 5. Time evolution of BASIL water vapor mixing ratio from 1805 UTC 1 Oct to 0825 UTC 2 Oct 2005, with contour lines of MM5 potential vorticity (magenta), equivalent potential temperature (gray and black), and ECMWF tropopause height (2×10^{-6} m^2 s^{-1} K kg^{-1} surface; yellow). Vertical wind velocity w is illustrated as white arrows, with arrow lengths proportional to log w.

A wave activity is also visible in the MM5 output. Specifically, the MM5 high-resolution (1 km) simulation centered over BASIL (Fig. 6) shows the pressure perturbation field at 2030 UTC 1 October 2005 at an altitude of 5.5 km (red lines), which highlights the wave structure of this field. Isolines are oriented along the northwest–southeast direction, whereas throats in these isolines are oriented normally to this direction; this indicates that phase direction of waves is northwest–southeast (light blue line) and that wave fronts (dashed black lines) are approximately northeast–southwest oriented.

The wave activity is also confirmed by the MM5 output of both w and θ_e in Fig. 5. The presence of an intense wave activity at these levels is shown by the alternation of cells with positive and negative values of w; isolines of θ_e also suggest a strong stable stratification (i.e., fluid density decreasing with altitude), which is a suitable condition for gravity wave propagation. Moreover, for altitudes above 4 km, θ_e appears to be modulated by the wave activity. To properly highlight wave structures, MM5 data shown in Fig. 6 and those for vertical wind velocity and equivalent potential temperature illustrated in Fig. 5 are obtained from a model simulation performed with a horizontal resolution of 1 km.

The lack of microbarograph data does not allows for a rigorous vector analysis; therefore, a coarse analysis of the wave parameters is performed by using the lidar measurements of the water vapor mixing ratio, radiosonde soundings, and MM5 model output. Additionally, lidar measurements of particle backscatter are considered to reveal and interpret cloud formation mechanisms.

Gravity wave wavelength can be inferred from the MM5 simulation in Fig. 6, suggesting a value of 20–30 km, which is obtained as the separation of two consecutive wave fronts. As a result of gravity wave propagation, high-frequency oscillations with an amplitude of 200 m are found in the altitude region 2–3.25 km in the vertical profile of temperature (Fig. 7) provided by the upper-air sounding released at 2351 UTC from the nearby CNR IMAA station. This figure also illustrates the simultaneous temperature profile from BASIL (vertical resolution of 30–150 m and temporal resolution of 5 min), which reveals similar oscillations in the same altitude region.

Statically stable environments, such as the nocturnal boundary layer, support gravity wave propagation. Wave frequencies for internal gravity waves must be at an altitude less than the Brunt–Väisälä frequency, or buoyancy frequency

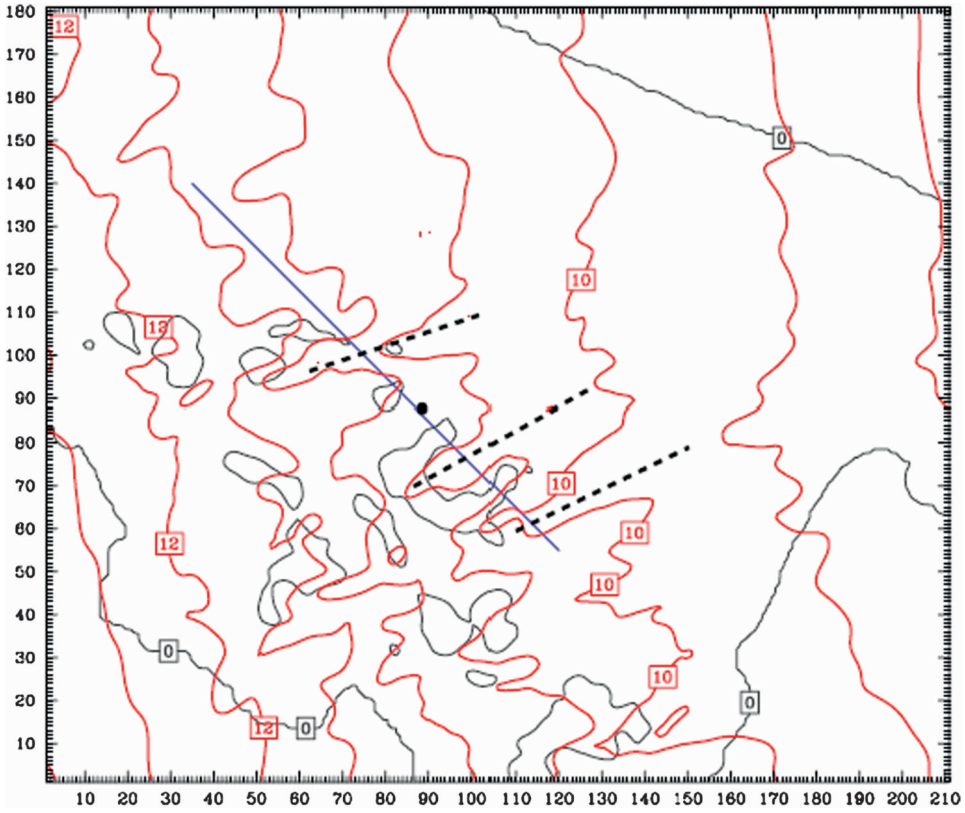

FIG. 6. MM5 simulation pressure perturbation field (contour interval = 0.5 hPa) at 2030 UTC 1 Oct 2005 at an altitude of 5.5 km. The gray isolines represent the orography (step = 1000 m), with the level 0 isoline highlighting the cost line. On the x and y axes, distances are reported in km. The light blue line indicates the phase direction of waves (northwest–southeast direction), whereas dashed black lines represent wave fronts. The lidar location is indicated by the black dot.

$$N_{\mathrm{BV}} = \sqrt{\frac{g}{\theta_v}\frac{\partial \theta_v}{\partial z}}, \tag{10}$$

where θ_v is the virtual potential temperature and g is the gravity acceleration at the surface.

Figure 8 illustrates the time evolution of the Brunt–Väisälä frequency as obtained from lidar measurements of potential temperature for the same 14.5-h period as in Fig. 5. The vertical and temporal resolutions of the temperature data are 300 m and 10 min, respectively. In the altitude region where waves are observed (1.5–6 km), frequencies are found to be less than 1.8×10^{-2} Hz, which corresponds to wave periods in excess of 6 min.

Wave period and amplitude can be inferred from the wavy structure of the humidity filaments present in the lidar data of the water vapor mixing ratio (Fig. 5). Specifically, wave period is determined as the temporal separation between two wave maxima, whereas wave amplitude is determined as half the vertical distance between a wave minimum and maximum. Wave period and amplitude are found to be 35 min and 200 m, respectively. The wave period value is confirmed by MM5 vertical wind velocity data in Fig. 5 before 2100 UTC in the altitude region 2–3.5 km, where it can be obtained as a time separation of consecutive cells with positive (or negative) values of w. The wave period value is compatible with the already-reported Brunt–Väisälä values in the region of waves (in excess of 6 min). Phase velocity is estimated from the gravity wave period, as determined by lidar measurements, and the wavelength, as estimated from MM5 simulations, and it is found to be 10–14 m s^{-1}.

Figure 9 illustrates the lidar measurements of atmospheric temperature over the same 14.5-h period of Fig. 5. The vertical and temporal resolutions of the temperature data are 300 m and 10 min, respectively. Temperature data reproduce the tongue-shaped feature present in the humidity field, with colder temperatures observed within the dry-air tongue. Figure 10 illustrates the relative humidity field obtained from the simultaneous lidar measurements of the water vapor mixing

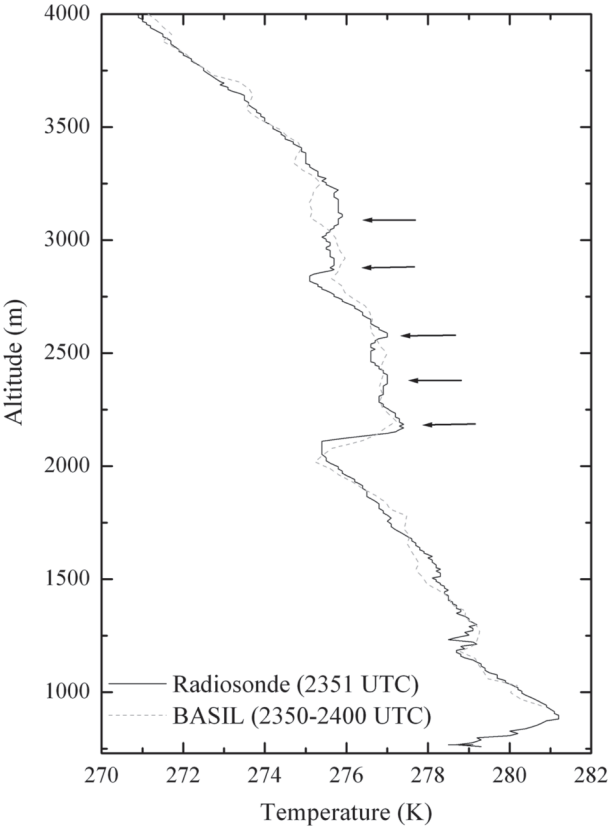

FIG. 7. Temperature profiles from BASIL and from the radiosonde released at 2351 UTC 1 Oct 2005 from CNR IMAA. Both BASIL and the radiosonde reveal oscillations in the altitude region 2–3.25 km.

ratio and atmospheric temperature. Here again, the vertical and temporal resolutions are 300 m and 10 min, respectively. When determining the lidar profiles of relative humidity, the pressure information from radiosondes is used. Four radiosondes were launched (1809 and 2351 UTC 1 October and 0556 and 1212 UTC 2 October 2005) that cover the 14.5-h period of these measurements. Pressure profiles at the times and altitudes of the lidar data are obtained from linear interpolation of the radiosonde data. Alternatively, pressure profiles are obtained from scaling surface pressure through the application of the hydrostatic equation. Relative humidity values as small as 0.5%–1% are observed within the upper lamina of the intruded stratospheric air, whereas the lower lamina (2–2.5 km) is characterized by relative humidity values of 5%–10%. Similar values of relative humidity as small as 0.5%–1% were also observed in intruded stratospheric air by D'Aulerio et al. (2004).

Clouds form as a result of humid air advection and uplift; uplift is determined by gravity wave activity. The presence of gravity wave–induced clouds is observed in Fig. 11, which illustrates the time evolution of particle backscatter at 355 nm. Clouds appear as out-of-range backscatter values between 1.6 and 2.0 km at ~2250 UTC and last until ~2340 UTC. Note that lidar measurements of the water vapor mixing ratio, temperature, and relative humidity reported in this paper (Figs. 4, 5, 9, 10) are performed inside and beyond the clouds because cloud optical thicknesses are small (not exceeding 0.2).

Horizontal advection of humid air is observed at levels were clouds are found to form (i.e., at 1.6–2.0 km). This is revealed by the increasing values present in the water vapor mixing ratio at these levels during the evening on 1 October (see Figs. 4, 5, 14). As a result of humid air advection and nighttime radiative cooling, relative humidity in the vertical region of 1.6–2.0 km increases from values of 20%–30% around 1800 UTC to values slightly less than 100% around 2250 UTC (Fig. 10). Clouds form when saturation conditions are reached. Then, after 2250 UTC, gravity waves contribute to the cloud formation process by providing the air uplift—with consequent adiabatic cooling—needed to reach and slightly exceed 100% relative humidity, which allows for water condensation onto aerosols and the formation of cloud particles. It is noteworthy that gravity waves are present also before 2250 UTC, but the air uplift associated with these waves before 2250 UTC does not lead to the formation of clouds because of the smaller relative humidity values of the air masses sampled at these times (see Figs. 11, 10).

b. Trajectory analysis

A Lagrangian trajectory model is used to identify the origin of the observed dry layer. The trajectory analysis is performed using the National Oceanic and Atmospheric Administration Air Resources Lab (NOAA/ARL) Hybrid Single Particle Lagrangian Integrated Trajectory (HYSPLIT) transport and dispersion model (Draxler and Rolph 2003). Meteorological data from the National Centers for Environmental Prediction (NCEP)–NCAR global reanalyses are used as model input. Figure 12 illustrates the backward trajectories ending at 1800 UTC 1 October 2005, the time when the lidar measurements were started and the elevated dry layer was first observed at an altitude of 6–7 km. The backward trajectories are ending at altitudes of 5, 5.5, and 6 km above ground level (AGL), and they are extending back in time for 96 h. The trajectories clearly reveal (Figs. 12a,b) that the air mass observed in Potenza at 5–6 km AGL descended from an altitude of 7–9 km AGL over Scandinavia. Additionally, forward trajectories starting in Potenza at 1800 UTC 1 October 2005 from altitudes

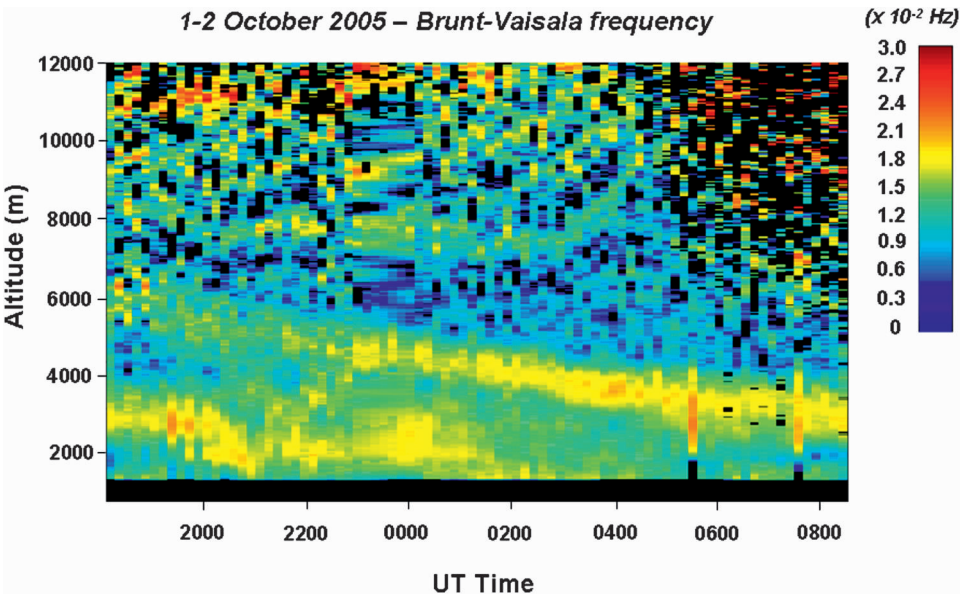

FIG. 8. Time evolution of the Brunt–Väisälä frequency (same time frame as in Fig. 5).

of 5–6 km AGL are found to descend to 4–5 km AGL in the following 12 h (Fig. 12c).

All the previously discussed trajectory results (Figs. 12a–c) confirm the descending trend of the stratospheric intruded air observed by lidar. The trajectories of the sounded air masses were also verified at a later time. Backward trajectories show that the air masses found at altitudes of 3.5–4.5 km AGL at 0000 UTC 2 October 2005 had moved 96 h earlier from an altitude of 5.5–7.5 km AGL, again over Scandinavia (Fig. 12d), whereas forward trajectories starting at the same time and altitudes are found to descend to 2.5–3.5 km AGL in the following 12 h (Fig. 12e), reproducing the air descending trend observed by lidar.

The HYSPLIT Lagrangian model has the possibility to track a variety of meteorological parameters along the backward/forward trajectories. Exploiting this model option, the variability of the water vapor mixing ratio along the back trajectories is determined. Specifically, the water vapor mixing ratio decreases along the back

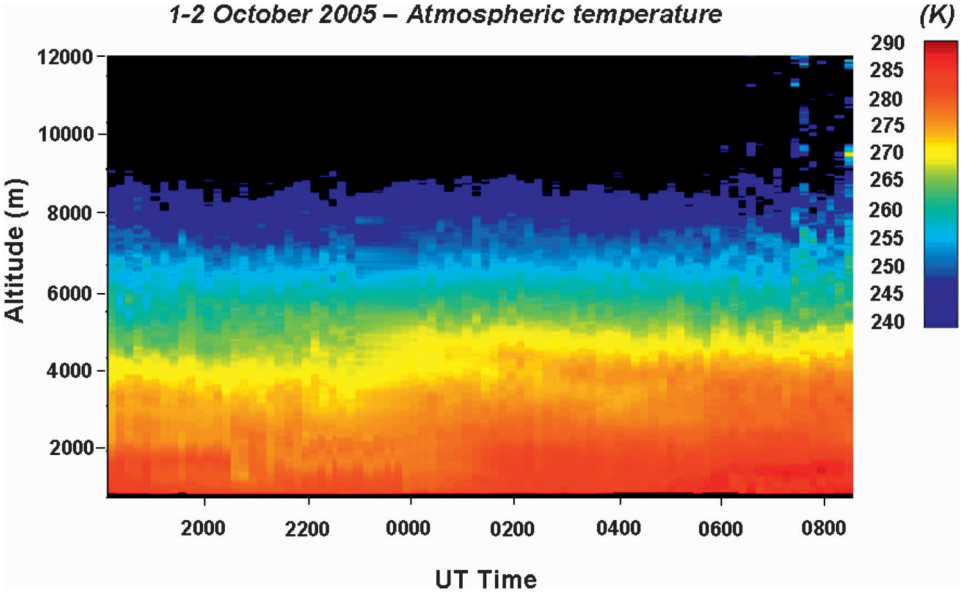

FIG. 9. Time evolution of BASIL atmospheric temperature (same time frame as in Fig. 5).

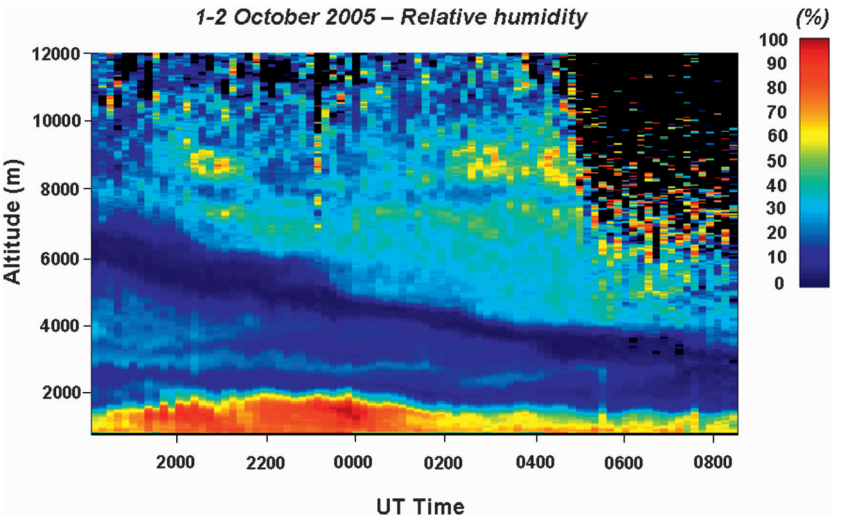

FIG. 10. Time evolution of BASIL relative humidity (same time frame as in Fig. 5).

trajectories from values of 0.065, 0.044, and 0.028 g kg^{-1} at 6, 6.5, and 7 km AGL, respectively, found by the HYSPLIT model at 1800 UTC 1 October 2005 to values in the range 0.005–0.03 g kg^{-1} found 36 h earlier in the altitude region of 8–10 km AGL. This result suggests the occurrence of a progressive mixing of the air masses penetrating down through the troposphere.

Furthermore, trajectory analysis results in Fig. 13 reveal that the dry layer at 2–2.5 km AGL is formed by air masses that have stationed at almost the same altitude in the previous 72 h; therefore, it did not intrude from higher levels. This result supports the hypothesis that the lower dry-air lamina is not part of the air intruded from the stratosphere.

c. *Comparison of lidar versus MM5 and ECMWF*

1) WATER VAPOR MIXING RATIO

Comparisons in terms of the water vapor mixing ratio between lidar measurements and both the MM5 mesoscale and ECMWF global models are illustrated in Fig. 14, with the MM5 simulation in the top panel, the ECMWF analysis in the bottom panel, and the lidar measurements in both panels as contour lines. Model simulations cover the 48-h period from 1800 UTC 1 October 2005, whereas lidar measurements are reported only for the time interval when these are available (from 1805 UTC 1 October to 0215 UTC 3 October 2005). MM5 is able to simulate the presence of a dry

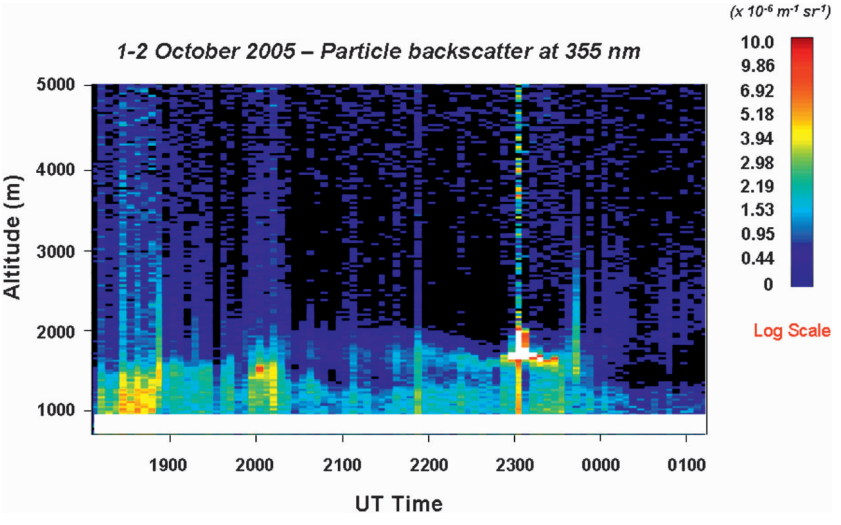

FIG. 11. Time evolution of BASIL particle backscatter at 355 nm in the time period from 1805 UTC 1 Oct to 0115 UTC 2 Oct 2005.

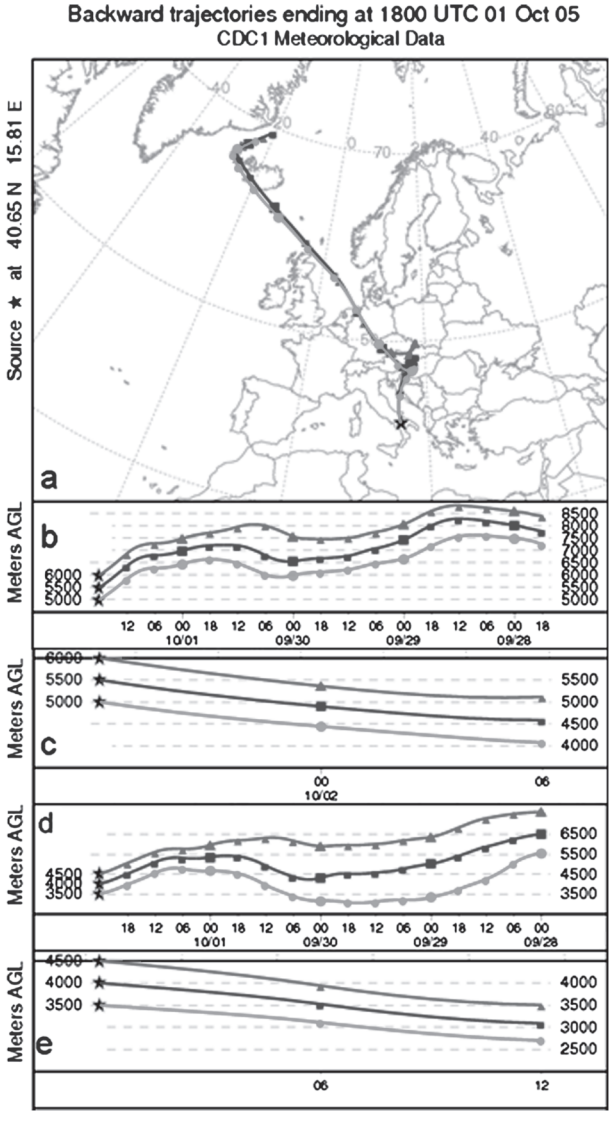

FIG. 12. Trajectory analysis: (a) geographical path of back trajectories ending at 5–6 km AGL; (b) time–height cross section of back trajectories ending at 5–6 km AGL; and (c) time–height cross section of forward trajectories starting at 5–6 km AGL. (a)–(c) 1800 UTC 1 Oct 2005. Time–height cross sections of (d) back trajectories ending at 3.5–4.5 km AGL and (e) forward trajectories starting at 3.5–4.5 km AGL at 0000 UTC 2 Oct 2005.

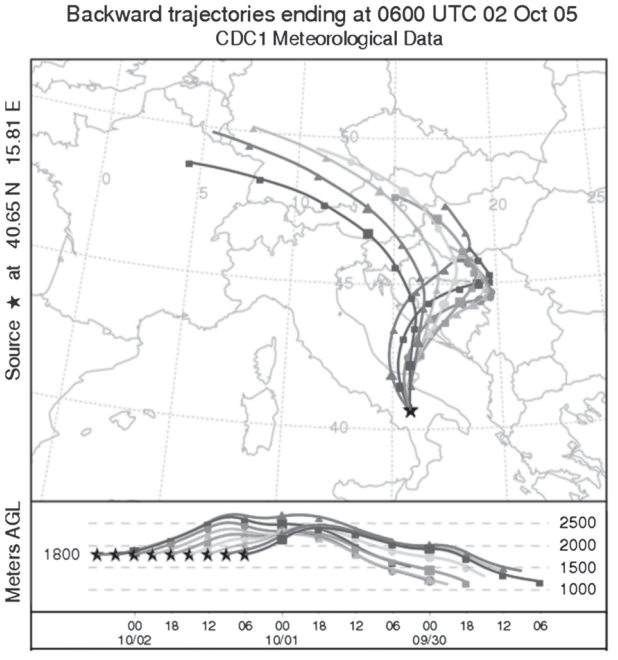

FIG. 13. Trajectory analysis: (a) geographical path and (b) time–height cross section of back trajectories ending at 1.8 km AGL at 0600 UTC 2 Oct 2005.

layer, which subsides and reaches an altitude of ~3 km at approximately 0900 UTC 2 October. This result compares reasonably well with the time series measured by BASIL. Specifically, lidar measurements indicate that the dry-layer tongue penetrates in the troposphere ~1 km deeper than predicted by MM5. Additionally, lidar data indicate that the dry-layer tongue persists for a longer period (2–3 h) than predicted by MM5. MM5 does not appear to be able to reproduce the very low water vapor mixing ratios inside the filament: at around a 3-km altitude, the modeled water vapor mixing ratio is 2–3 times larger than the lidar measurements, whereas deviations between lidar and MM5 are only a factor of 1.5–2 in the upper portion of the layer. These results reveal a reasonably good capability of the MM5 model to simulate the evolution of the dry-air tongue intruding from the stratosphere.

On the other hand, the ECMWF analysis of the water vapor mixing ratio (Fig. 14, bottom) shows a poor agreement with both the MM5 simulation and lidar data. ECMWF fails to predict the wedge shape of the intruded dry-air tongue and its deep penetration into the lower troposphere. Values of the water vapor mixing ratio inside the dry layer are remarkably higher than those measured by lidar or produced by MM5. Additionally, ECMWF output appears to be vertically mismatched with respect to both MM5 and lidar measurements, with the latter two detecting the dry-layer tongue 1–3 km deeper in the troposphere than ECMWF.

These results reveal that the higher-resolution model allows to better simulate dry stratospheric air intrusion episodes associated with tropopause folding events, as well as to predict their destruction by turbulence. However, improvements in the simulation could probably come from real-time three-dimensional variational data assimilation (3DVAR) or 4DVAR assimilations of lidar measurements of the water vapor mixing ratio in this model.

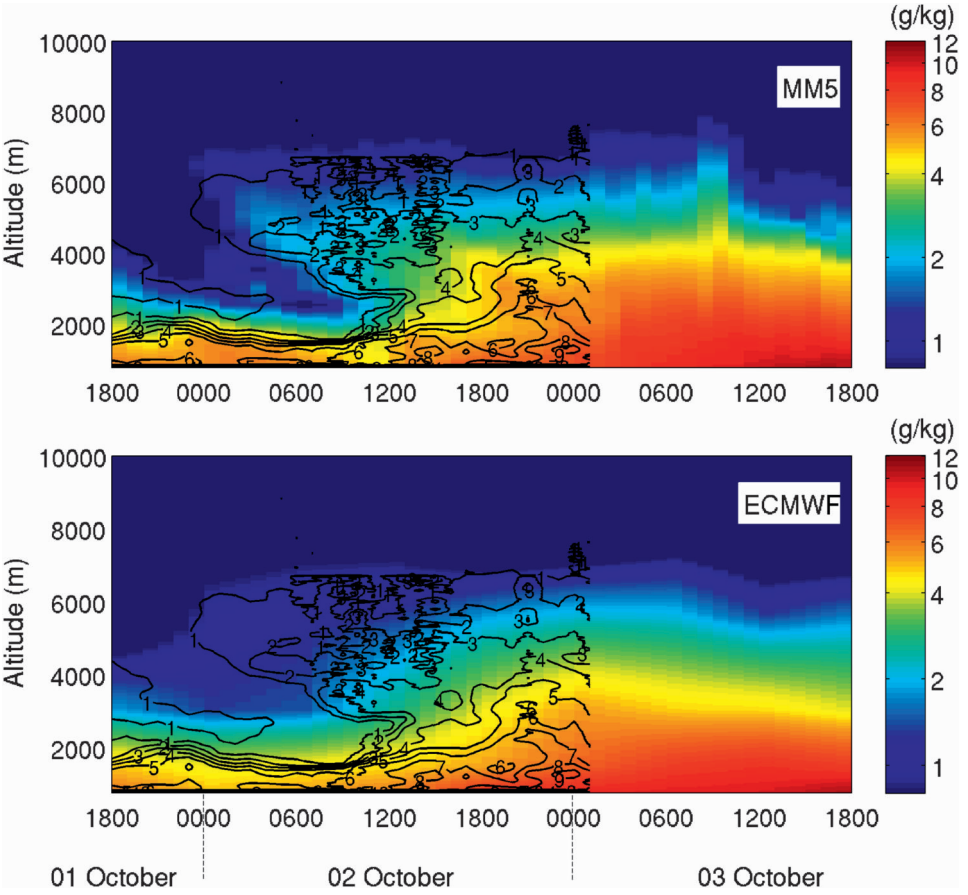

FIG. 14. (top) MM5 and (bottom) ECMWF simulation of the water vapor mixing ratio. Models are initiated at 1800 UTC 1 Oct 2005 and run for 48 h. Raman lidar measurements of the water vapor mixing ratio are also illustrated for comparison (black contour lines).

2) POTENTIAL TEMPERATURE

The comparison between MM5 output and lidar measurements in terms of potential temperature is illustrated in Fig. 15, where lidar measurements are shown as a color map and MM5 data are illustrated as contour lines. The figure covers the period of 1800 UTC 1 October to 0800 UTC 2 October 2005. When determining lidar profiles of potential temperature, pressure information from radiosondes is used, with pressure profiles at the times and altitudes of the lidar data obtained from linear interpolation of the radiosonde data. The vertical and temporal resolutions of the lidar data are the same as in Fig. 9 (300 m and 10 min, respectively). The model sampling time is 1 h, while vertical resolution is few meters in the PBL, decreasing upward in the free troposphere. Lidar data clearly reveal the variability of potential temperature associated with the stratospheric intrusion episode, which reproduces the tongue-shaped feature present in the humidity field, with lower potential temperature values observed within the dry-air tongue. This variability is only partially reproduced by MM5. Additionally, lidar measurements of potential temperature show the presence of a marked gradient in the altitude region of 1.4–1.8 km, which identifies the residual layer top (i.e., the top of the statically neutral region). Potential temperature from MM5 does not show as clear of a signal as the one detected by lidar, but a stratification in the lower layers is clearly reproduced as well as a change in the stratification rate from 1 to 2 October.

3) POTENTIAL VORTICITY

PV is defined (Ertel 1942) as

$$\mathrm{PV} = \frac{\zeta_\theta + f}{-\frac{1}{g}\left(\frac{\partial p}{\partial \theta}\right)}, \tag{11}$$

where ζ_θ is the vertical component of relative vorticity on an isentropic surface, f is the Coriolis parameter, and θ is the potential temperature.

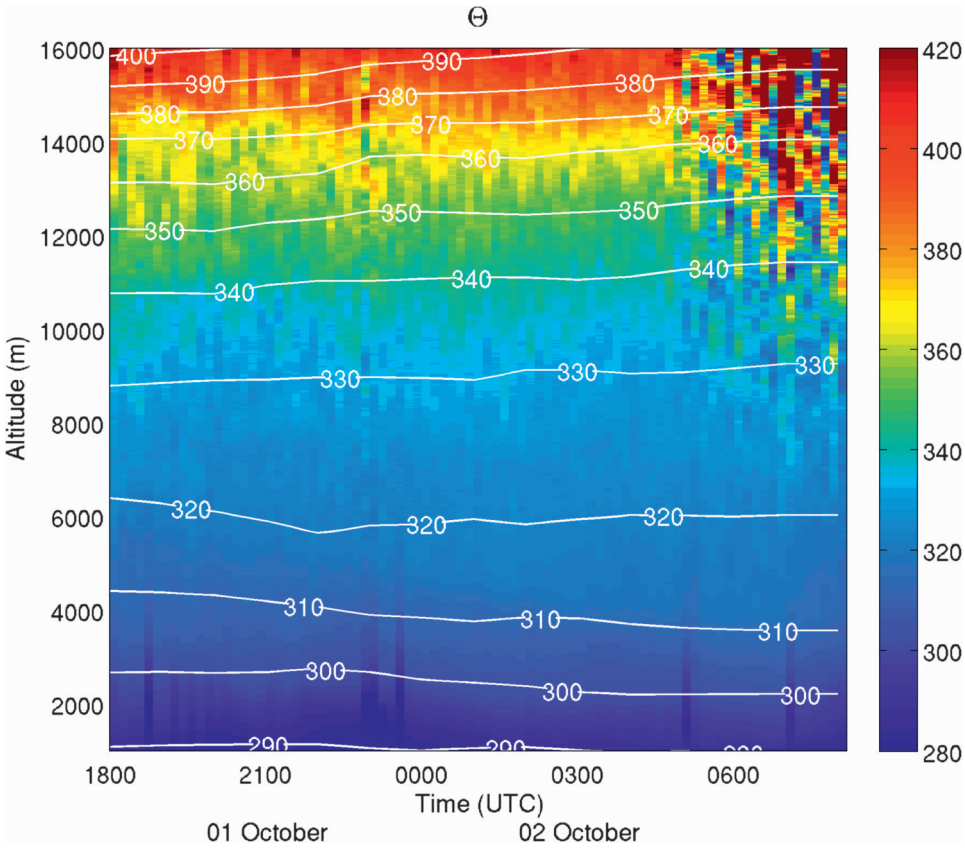

FIG. 15. Comparison of Raman lidar (color map) and MM5 simulation (white contour lines) in terms of potential temperature.

PV is a widely used parameter to estimate the tropopause altitude and quantify the degree of mixing/exchange between the troposphere and stratosphere. In extratropical regions, the tropopause altitude is in very good correspondence with a surface of constant PV with a value of 2×10^{-6} m^2 s^{-1} K kg^{-1} (Hoerling et al. 1991).

PV from MM5 for the same 14-h period of Fig. 15 is illustrated in Fig. 16 as gray and black contour lines, whereas the one for ECMWF is shown as white contour lines. Both models locate reasonably well, both spatially and temporally, the PV gradients associated with the stratospheric intrusion episode, but this is better defined by MM5. However, values of PV inside the dry-air tongue for both models (not exceeding 2×10^{-6} and 1.5×10^{-6} m^2 s^{-1} K kg^{-1} for MM5 and ECMWF, respectively) are found to be slightly lower than those usually found in intruded stratospheric air (D'Aulerio et al. 2004).

A combined lidar–MM5 estimate of PV (color map in Fig. 16) can also be obtained through expression (11), using lidar measurements of potential temperature (vertical resolution of 300 m and temporal resolution of 10 min) and model data for all other parameters. The PV increase associated with the stratospheric intrusion episode is better reproduced by the lidar-assisted MM5 estimate than by either MM5 alone or ECMWF, with larger PV values within the dry-air tongue (up to 2.5–3.0×10^{-6} m^2 s^{-1} K kg^{-1}). The uncertainty affecting the lidar-aided MM5 estimates of PV, as a result of the random uncertainty affecting lidar measurements of potential temperature, is 10%–15% in the 3–7-km region. However, lidar-aided MM5 estimates of PV rely on MM5 model vorticity data, which can be affected by both systematic and statistical uncertainties. These may ultimately induce an additional error on the estimate of PV (~5%).

6. Summary

The Raman lidar system BASIL has been used to study a dry stratospheric intrusion episode associated with a tropopause folding event. Lidar measurements of water vapor mixing ratio and temperature carried out from 1 to 3 October 2005 revealed the presence of a cold dry-air tongue descending from the upper troposphere deep into the lower troposphere. Relative humidity

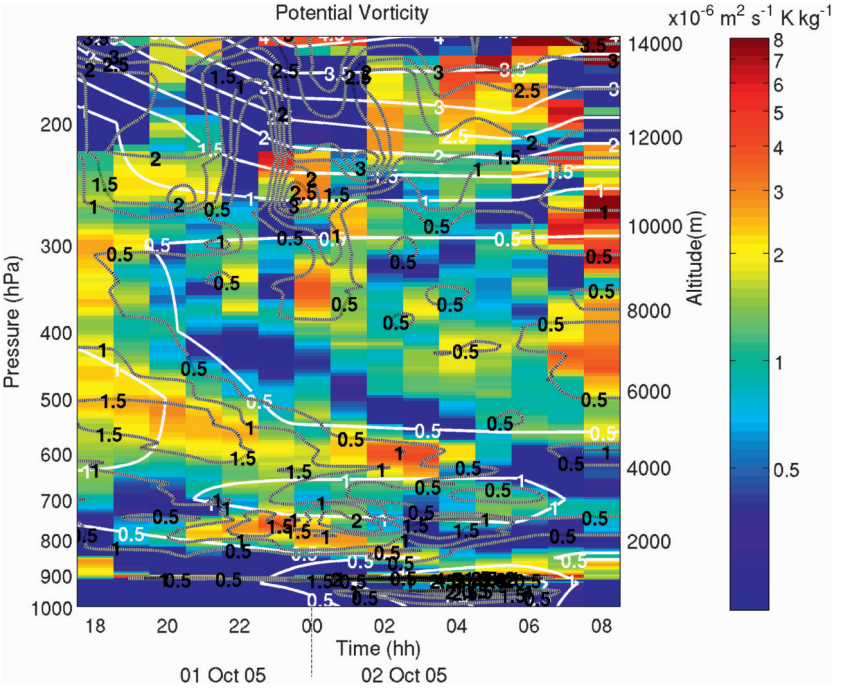

FIG. 16. Lidar-assisted estimate of PV based on lidar measurements of potential temperature and MM5 model data for all other parameters. MM5 and ECMWF simulations of potential vorticity are illustrated for comparison as gray–black and white contour lines, respectively.

values as small as 0.5%–1% were observed within the intruded air. The stratospheric origin of the dry-air tongue was verified through a Lagrangian trajectory model. Lidar measurements also allowed monitoring of the presence of propagating gravity waves beneath the dry layer, possibly generated by the subsiding heavy dry air, which generates density fluctuations. Gravity waves are found to trigger the formation of low-level clouds. This study demonstrates that Raman lidars with water vapor and temperature measurement capabilities are very suitable tools to resolve the spatial and temporal scales typical of stratosphere–troposphere exchange mechanisms.

Lidar measurements have been compared with the outputs of both the MM5 and ECMWF models in terms of water vapor mixing ratio. The MM5 output compares reasonably well with the measurements by BASIL, both spatially and temporally, properly simulating the dynamical processes that generate the narrow dry filament, whereas ECMWF output reveals a poorer agreement with observations. The agreement between lidar observations and MM5 simulations, in terms of potential temperature, is good. However, the variability of potential temperature associated with the stratospheric intrusion event is only partially reproduced by MM5. For what concerns potential vorticity, its variability associated with the stratospheric intrusion event is reproduced by both MM5 and ECMWF. Nevertheless, an improvement in MM5 capability to reveal this variability is obtained if lidar measurements are used for estimating potential temperature, besides a general increase of the noisiness of the data.

Results in this paper reveal the large potential of coupling/assimilating Raman lidar measurements of water vapor mixing ratio both in global- and high-resolution mesoscale models. Additionally, the demonstrated capability of Raman lidars to provide measurements that—in conjunction with high-resolution mesoscale models—allow monitoring the variability of potential vorticity with high time and space resolution makes them ideal tools to study tropopause folding events and monitor baroclinic instabilities.

Acknowledgments. We wish to gratefully acknowledge NOAA/ARL for the provision of the HYSPLIT transport and dispersion model (available online at http://www.arl.noaa.gov/ready.html) used in this publication. We wish to thank CNR IMAA for the SEVIRI quick-look images used in the publication and for the provision of radiosonde data. NCAR is also acknowledged for the MM5 model.

REFERENCES

Appenzeller, C., and H. C. Davies, 1992: Structure of stratospheric intrusions into the troposphere. *Nature,* **358,** 570–572.

Avila, G., J. M. Fernández, B. Maté, G. Tejeda, and S. Montero, 1999: Ro-vibrational Raman cross sections of water vapor in the OH stretching region. *J. Mol. Spectrosc.,* **196,** 77–92.

Behrendt, A., 2005: Temperature measurements with lidar. *Lidar: Range-Resolved Optical Remote Sensing of the Atmosphere,* C. Weitkamp, Ed., Optical Sciences, Vol. 102, Springer, 273–305.

——, and J. Reichardt, 2000: Atmospheric temperature profiling in the presence of clouds with a pure rotational Raman lidar by use of an interference-filter-based polychromator. *Appl. Opt.,* **39,** 1372–1378.

Bertin, F., B. Campistron, J. L. Caccia, and R. Wilson, 2001: Mixing processes in the tropopause folding observed by a network of ST radar and lidar. *Ann. Geophys.,* **19,** 953–963.

Brewer, A. M., 1949: Evidence for a world circulation provided by the measurements of helium and water vapor distribution in the stratosphere. *Quart. J. Roy. Meteor. Soc.,* **75,** 351–363.

Cristofanelli, P., and Coauthors, 2003: Stratosphere-to-troposphere transport: A model and method evaluation. *J. Geophys. Res.,* **108,** 8525, doi:10.1029/2002JD002600.

D'Aulerio, P., F. Fierli, F. Congeduti, and G. Redaelli, 2004: Analysis of water vapor LIDAR measurements during the MAP campaign: Evidence of sub-structures of stratospheric intrusions. *Atmos. Chem. Phys. Discuss.,* **4,** 8327–8355.

Di Girolamo, P., R. Marchese, D. N. Whiteman, and B. B. Demoz, 2004: Rotational Raman Lidar measurements of atmospheric temperature in the UV. *Geophys. Res. Lett.,* **31,** L01106, doi:10.1029/2003GL018342.

——, A. Behrendt, and V. Wulfmeyer, 2006: Spaceborne profiling of atmospheric temperature and particle extinction with pure rotational Raman lidar and of relative humidity in combination with differential absorption lidar: Performance simulations. *Appl. Opt.,* **45,** 2474–2494.

——, ——, C. Kiemle, V. Wulfmeyer, H. Bauer, D. Summa, A. Dörnbrack, and G. Ehret, 2008: Simulation of satellite water vapour lidar measurements: Performance assessment under real atmospheric conditions. *Remote Sens. Environ.,* **112,** 1552–1568.

Donovan, D. P., J. A. Whiteway, and A. I. Carswell, 1993: Correction for nonlinear photon-counting effects in lidar systems. *Appl. Opt.,* **32,** 6742–6753.

Draxler, R. R., and G. D. Rolph, cited 2003: HYSPLIT (Hybrid Single-Particle Lagrangian Integrated Trajectory) Model. NOAA Air Resources Laboratory. [Available online at http://www.arl.noaa.gov/ready/open/hysplit4.html.]

Dudhia, J., 1993: A non-hydrostatic version of the Penn State–NCAR Mesoscale Model: Validation tests and simulation of an Atlantic cyclone and cold front. *Mon. Wea. Rev.,* **121,** 1493–1513.

Ertel, H., 1942: Ein Neuer hydrodynamischer Wirbelsatz. *Meteorol. Z.,* **59,** 271–281.

Ferretti, R., T. Paolucci, W. Zheng, G. Visconti, and P. Bonelli, 2000: Analyses of the precipitation pattern on the Alpine region using different cumulus convection parameterizations. *J. Appl. Meteor.,* **39,** 182–200.

Fiorucci, I., and Coauthors, 2008: Measurements of low amounts of precipitable water vapor by millimeter wave spectroscopy: An intercomparison with radiosonde, Raman lidar, and Fourier transform infrared data. *J. Geophys. Res.,* **113,** D14314, doi:10.1029/2008JD009831.

Flentje, H., A. Dörnbrack, G. Ehret, A. Fix, C. Kiemle, G. Poberaj, and M. Wirth, 2005: Water vapor heterogeneity related to tropopause folds over the North Atlantic revealed by airborne water vapor differential absorption lidar. *J. Geophys. Res.,* **110,** D03115, doi:10.1029/2004JD004957.

Forster, C., and V. Wirth, 2000: Radiative decay of idealized stratospheric filaments in the troposphere. *J. Geophys. Res.,* **105,** 10 169–10 184.

Galani, E., D. Balis, P. Zanis, C. Zerefos, A. Papayannis, H. Wernli, and E. Gerasopoulos, 2003: Observations of stratosphere-to-troposphere transport events over the eastern Mediterranean using a ground-based lidar system. *J. Geophys. Res.,* **108,** 8527, doi:10.1029/2002JD002596.

Goering, M. A., W. A. Gallus Jr., M. A. Olsen, and J. L. Stanford, 2001: Role of stratospheric air in a severe weather event: Analysis of potential vorticity and total ozone. *J. Geophys. Res.,* **106,** 11 813–11 823.

Grell, G. A., J. Dudhia, and D. R. Stauffer, 1994: A description of the fifth-generation Penn State/NCAR mesoscale model (MM5). NCAR Tech. Note NCAR/TN-398+STR, 128 pp.

Griaznov, V., I. Veselovskii, P. Di Girolamo, M. Korenskii, and D. Summa, 2007: Spatial distribution of doubly scattered polarized laser radiation in the focal plane of a lidar receiver. *Appl. Opt.,* **46,** 6821–6830.

Grzeschik, M., and Coauthors, 2008: Four-dimensional variational data analysis of water vapor Raman lidar data and their impact on mesoscale forecasts. *J. Atmos. Oceanic Technol.,* **25,** 1437–1453.

Hoerling, M. P., T. K. Schaack, and A. J. Lenzen, 1991: Global objective tropopause analysis. *Mon. Wea. Rev.,* **119,** 1816–1831.

Hoinka, K. P., E. Richard, G. Poberaj, R. Busen, J.-L. Caccia, A. Fix, and H. Mannstein, 2003: Analysis of a potential-vorticity streamer crossing the Alps during MAP IOP 15 on 6 November 1999. *Quart. J. Roy. Meteor. Soc.,* **129,** 609–632.

Holton, J. R., P. H. Haynes, E. M. McIntyre, A. R. Douglass, R. B. Rood, and L. Pfister, 1995: Stratosphere-troposphere exchange. *Rev. Geophys.,* **33,** 403–439.

IEC, 2001: Safety of laser products—Part 1: Equipment classification, requirements and user's guide, ed. 1.2. International Electrotechnical Commission IEC 60825-1, 115 pp.

Kain, J. S., and J. M. Fritsch, 1993: Convective parametrization for mesoscale models: The Kain–Fritsch scheme. *The Representation of Cumulus Convection in Numerical Models, Meteor. Monogr.,* No. 24, Amer. Meteor. Soc., 165–170.

Koch, S. E., and C. Lu, 2006: The generation of gravity waves in unbalanced jet streams. *Geophysical Research Abstracts,* Vol. 8, Abstract 10659. [Available online at http://www.cosis.net/abstracts/EGU06/10659/EGU06-J-10659-1.pdf.]

Massacand, A. C., H. Wernli, and H. C. Davies, 2001: Influence of upstream diabatic heating upon an Alpine event of heavy precipitation. *Mon. Wea. Rev.,* **129,** 2822–2828.

Mattis, I., and Coauthors, 2002: Relative-humidity profiling in the troposphere with a Raman lidar. *Appl. Opt.,* **41,** 6451–6462.

Mielke, B., 2005: Analog + photon counting. Licel Tech. Note, 10 pp. [Available online at http://www.licel.com/analogpc.pdf.]

Neiman, P. J., F. M. Ralph, R. L. Weber, T. Uttal, L. B. Nance, and D. H. Levinson, 2001: Observations of nonclassical frontal propagation and frontally forced gravity waves adjacent to steep topography. *Mon. Wea. Rev.,* **129,** 2633–2659.

Paolucci, T., L. Bernardini, R. Ferretti, and G. Visconti, 1999: Operational forecast using a high resolution limited area model. *Nuovo Cimento,* **22,** 727–736.

Reid, S. J., and G. Vaughan, 1991: Lamination in ozone profiles in the lower stratosphere. *Quart. J. Roy. Meteor. Soc.,* **117,** 825–844.

Reisner, J., R. Rasmussen, and R. Bruintjes, 1998: Explicit forecasting of supercooled liquid water in winter storms using the MM5 mesoscale model. *Quart. J. Roy. Meteor. Soc.,* **124,** 1071–1107.

Roelofs, G. J., A. S. Kentarchos, T. Trickl, A. Stohl, W. J. Collins, R. A. Crowther, and D. Hauglustaine, 2003: Intercomparison of tropospheric ozone models: Ozone transport in a complex tropopause folding event. *J. Geophys. Res.,* **108,** 8529, doi:10.1029/2003JD003462.

Serafin, S., and R. Ferretti, 2007: Sensitivity of a mesoscale model to microphysical parameterizations in the MAP SOP events IOP2b and IOP8. *J. Appl. Meteor. Climatol.,* **46,** 1438–1454.

Shapiro, M. A., 1980: Turbulent mixing within tropopause folds as a mechanism for the exchange of chemical constituents between the stratosphere and troposphere. *J. Atmos. Sci.,* **37,** 994–1004.

Stohl, A., and T. Trickl, 1999: A textbook example of long-range transport: Simultaneous observation of ozone maxima of stratospheric and North American origin in the free troposphere over Europe. *J. Geophys. Res.,* **104,** 30 445–30 462.

——, and Coauthors, 2003: Stratosphere-troposphere exchange: A review, and what we have learned from STACCATO. *J. Geophys. Res.,* **108,** 8516, doi:10.1029/2002JD002490.

Troen, I. B., and L. Mahrt, 1986: A simple model of the atmospheric boundary layer: Sensitivity to surface evaporation. *Bound.-Layer Meteor.,* **37,** 129–148.

Whiteman, D. N., 2003a: Examination of the traditional Raman lidar technique. I. Evaluating the temperature-dependent lidar equations. *Appl. Opt.,* **42,** 2571–2592.

——, 2003b: Examination of the traditional Raman lidar technique. II. Evaluating the ratios for water vapor and aerosols. *Appl. Opt.,* **42,** 2593–2608.

——, S. H. Melfi, and R. A. Ferrare, 1992: Raman lidar system for the measurement of water vapor and aerosols in the Earth's atmosphere. *Appl. Opt.,* **31,** 3068–3082.

——, and Coauthors, 2006: Raman lidar measurements during the International H_2O Project. I. Instrumentation and analysis techniques. *J. Atmos. Oceanic Technol.,* **23,** 157–169.

WMO, 2002: General meteorological standards and recommended practices. WMO Tech. Regulations WMO-No. 49, corrigendum.

Wulfmeyer, V., H. S. Bauer, M. Grzeschik, A. Behrendt, F. Vandenberghe, E. V. Browell, S. Ismail, and R. A. Ferrare, 2006: Four-dimensional variational assimilation of water vapor differential absorption lidar data: The first case study within IHOP 2002. *Mon. Wea. Rev.,* **134,** 209–230.

Zanis, P., and Coauthors, 2003: Forecast, observation and modelling of a deep stratospheric intrusion event over Europe. *Atmos. Chem. Phys.,* **3,** 763–777.

Zhang, F., S. E. Koch, C. A. Davis, and M. L. Kaplan, 2001: Wavelet analysis and the governing dynamics of a large-amplitde mesoscae gravity-wave event along the East Coast of the United States. *Quart. J. Roy. Meteor. Soc.,* **127,** 2209–2245.